Arabian Journal for Science and Engineering (2024) 49:8679–8698
https://doi.org/10.1007/s13369-023-08402-7

RESEARCH ARTICLE-PETROLEUM ENGINEERING

Pore Structure Characterization of Lacustrine Shale and its Coupling Relationship with Sedimentary Structure from the Upper Cretaceous Qingshankou Formation, Southern Songliao Basin, NE China

Lei Li[1,2] · Zhidong Bao[1,2] · Zhongcheng Li[3] · Li Chen[3] · Yonggang Zhao[4] · Hongyu Zhao[3] · Jianyi Wang[3] · Yu He[3] · Shuyue Ban[1,2]

Received: 2 April 2023 / Accepted: 21 June 2023 / Published online: 28 January 2024

Abstract

Characterizing the microscopic pore systems in shale reservoirs is crucial for understanding their impact on shale oil and gas enrichment. Although significant strides have been made in understanding the pore structure characteristics, research on pore structures related to small-scale sedimentary structures remains limited. This study investigated the multi-scale nanopore structure characterization and its coupling relationship with sedimentary structures using comprehensive analyses of cores, field-emission scanning electron microscopy, and gas (CO2 and N2) physisorption quantification from the Upper Cretaceous Qingshankou Formation, Southern Songliao Basin, NE China. Three lithofacies were identified based on sedimentary structures: wavy laminated shale, horizontally laminated shale, and homogeneously laminated shale. Both organic and inorganic pores (interparticle pores and intraparticle pores) are generally present in shale samples. The pore size distribution displays a multi-peak pattern, with mesopores contributing to approximately 57% of the total pore volume, micropores contributing to about 31%, and macropores accounting for a small portion of the total pore volume. The pore evolution of different lithofacies shales varies due to the influence of clay minerals, quartz content, and total organic carbon (TOC) content, resulting in the substantial heterogeneity and complex pore structure characteristics of existing reservoirs. Additionally, wavy laminated shales are more favorable to lacustrine shale exploration than other lithofacies. This study offers an enhanced methodology for determining which lithofacies may be most advantageous for future shale oil exploitation.

Keywords Sedimentary structure · Lithofacies · Nanopore structure · Fractal dimension · Lacustrine shale · Songliao Basin

1 Introduction

Since the beginning of the twenty-first century, shale oil and gas, classified as unconventional oil and gas resources, have increasingly become significant in the international energy market [1–3]. Successfully produced shale oil and gas reservoirs have a complex microstructure and substantial heterogeneity and exist pervasively in most of the significant petroliferous basins in China, including the Ordos, Sichuan, Tarim, and Songliao Basins [4–7]. Shale oil is an essential unconventional resource, primarily found in micro-/nanopores and fractures of shale reservoirs in adsorption and free states [8–12]. The micro-/nanopores and microfractures with pore sizes larger than 30 nm are the main reservoir space for shale oil and gas [13]. Whether a shale reservoir can achieve enrichment and high production depends on its multi-scale nanopore structure [1, 14–17].

With the increasing focus on unconventional nanoreservoir research, academic and industrial communities have paid greater attention to the small-scale sedimentary structures of shale. The main areas of interest include rock structure and microfabric [18–20], material composition and its changes

✉ Zhidong Bao
baozhd@cup.edu.cn

Lei Li
leili@student.cup.edu.cn

1 College of Geosciences, China University of Petroleum-Beijing, Beijing 102249, China

2 State Key Laboratory of Petroleum Resource and Prospecting, China University of Petroleum-Beijing, Beijing 102249, China

3 Research Institute of Exploration and Development, PetroChina Jilin Oilfield Company, Songyuan 138000, China

4 College of Earth Sciences and Engineering, Xi'an Shiyou University, Xi'an 710065, Shaanxi, China

[21, 22], diagenetic heterogeneity [4, 23], and the influence on physical properties, gas content, and development engineering measures [16, 24]. However, small-scale sedimentary structures can lead to differences in large-scale physical properties and pore structures [18, 25]. Further research is needed to reveal the impact of sedimentary structures on reservoir quality. Shale pores have recently been studied using multiple characterization methods based on multidisciplinary approaches, including direct observation, small molecule fluid injection, and ray detection [14, 24]. High-resolution pore images can be obtained through the direct observation method, which allows for qualitative observation of pore development characteristics and extraction of pores. Additionally, this method enables quantitative analysis of pores' number, roundness, and porosity using relevant image analysis software, such as ImageJ [26, 27]. Small molecule fluid injection methods include low-pressure gas adsorption (CO_2 and N_2), high-pressure mercury injection, and gas expansion (helium porosity). These methods can characterize the full scale of micropores, mesopores, macropores, and microfractures in shale [28–30]. Ray detection technology employs optical, electron, and neutron rays, using CT scanning (nano-/micro-CT) methods and small-angle scattering to identify shale pore space [31, 32]. However, these multi-method characterization techniques primarily focus on comprehensively acquiring micropore-throat structure parameters. The emergence and rapid development of fractal theory provide theoretical support for studying shale pore irregularity and surface roughness [33–37]. The Frenkel–Halsey–Hill (FHH) model is the best computational model for obtaining the fractal dimension of mesopores and micropores in shale [37–39]. The fractal dimension can be calculated through low-pressure liquid–nitrogen adsorption experiments, and the fractal dimensions obtained using this method can adequately reflect the fractal characteristics of pores in shale [39–41].

In the Southern Songliao Basin of NE China, the Upper Cretaceous Qingshankou Formation contains lacustrine shales with significant potential for shale oil exploration [40, 42–44]. Previous studies have made notable progress investigating pore structure characteristics within the Qingshankou Formation. These studies have examined various aspects of the pore structure, including porosity, size distribution, connectivity, and other relevant parameters [40, 45]. Additionally, researchers have utilized advanced imaging techniques such as scanning electron microscopy (SEM), focused ion beam-scanning electron microscopy (FIB-SEM), and mercury intrusion porosimetry to characterize the pore network in these lacustrine shales [46–48]. However, while significant strides have been made in understanding the pore structure characteristics, more research has yet to explore the coupling relationship between pore structure and small-scale sedimentary structures within the Qingshankou Formation. This research aims to build upon the existing body of knowledge by further investigating the pore structure characteristics and their relationship with small-scale sedimentary structures. By doing so, we can provide a more comprehensive understanding of the reservoir properties, optimize exploration and development strategies, and contribute to the sustainable development of hydrocarbon resources in the Songliao Basin.

This study aims to (1) characterize the small-scale sedimentary structure of Upper Cretaceous Qingshankou Formation lacustrine shales in the Southern Songliao Basin; (2) examine the pore structure characteristics of these lacustrine shales; and (3) explore the relationship between pore structure and small-scale sedimentary structure. This provides an enhanced methodology for determining which lithofacies may be most advantageous for future shale oil extraction.

2 Geological Setting

The Songliao Basin is a large lacustrine hydrocarbon-bearing basin in northeast China [49–52] (Fig. 1a). This basin comprises four primary tectonic units: the central depression, southeast uplift, west slope, and southwest uplift [20, 33, 52] (Fig. 1b). The research area is in the southern part of the Songliao Basin's central depression, encompassing four secondary structural units: Honggang terrace, Fuxin uplift, Changling depression, and Huazijing terrace [53].

During the Upper Cretaceous period, a worldwide "greenhouse climate" prevailed, characterized by elevated sea levels and a lack of long-lasting ice sheets [54, 55]. Concurrently, one of East Asia's most extensive oil-rich non-marine basins, the Songliao Basin in Northeast China (Fig. 1a), evolved. The Qingshankou Formation contains shale oil strata with abundant total organic carbon (TOC) and high oil production potential, particularly near the base of its initial (lower) member [45]. The shale is abundant in type I organic matter and features a mature oil window. Preliminary evaluations indicate promising shale oil potential [40, 53]. The Qingshankou Formation serves as the primary sedimentary deposit in the basin [42]. The basin's southern area mainly features three sources: west, southwest, and southeast [45, 56] (Fig. 2a). The Songliao Basin rapidly subsided and expanded during the deposition of the Qingshankou Formation. It is a warm and wet lacustrine deposit that can be divided into the K_2qn^1, K_2qn^2, and K_2qn^3 members, from bottom to top (Fig. 2b). The lithology of the K_2qn^1 Member primarily comprises black mudstone oil shale, gray siltstone, small amounts of gray ostracod limestone, and fine gray sandstone [10, 53].

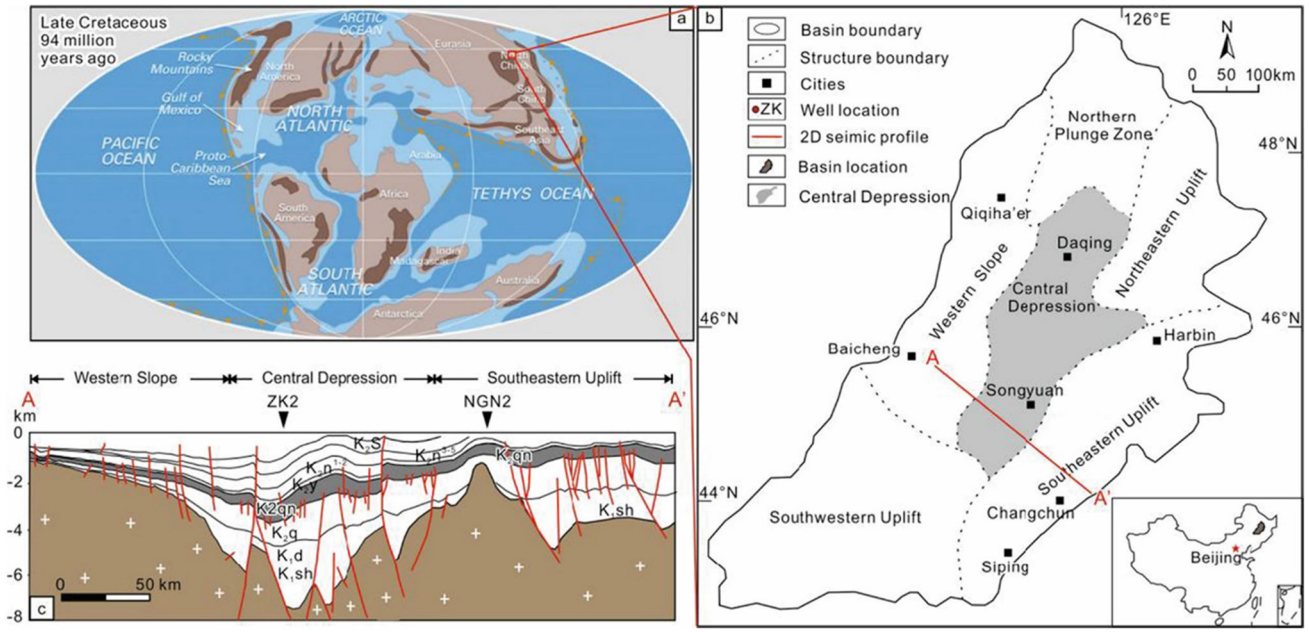

Fig. 1 **a** Late Cretaceous position of the Songliao Basin [54]. **b** Subdivisions within the Songliao Basin [49]. **c** Structural cross section of the Songliao Basin's central region, derived from regional seismic lines [49]

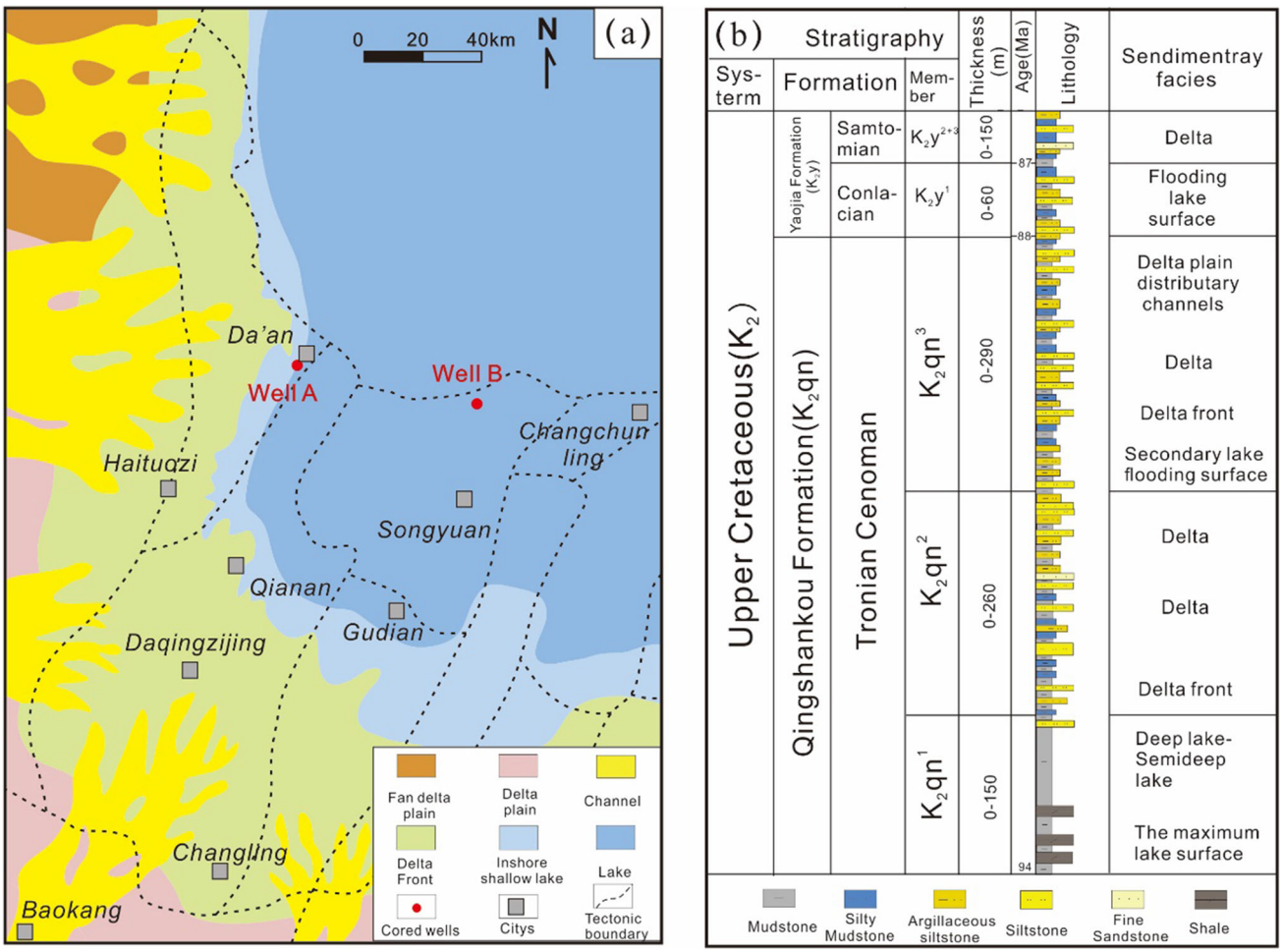

Fig. 2 **a** Study area and depositional settings of K_2qn^1 in the Songliao Basin [57]. **b** Stratigraphy and lithology of the Qingshankou Formation [45]

3 Experiments and Methods

3.1 Experimental Measurements

This study was based on detailed descriptions, photographs, laminae thickness measurements, and two wells' analysis of 42-m core records. Ten core samples were selected for experimental measurement based on typical lithofacies (Fig. 2a). The Ro value ranges between 0.41 and 1.27%, which falls within the oil window and in the peak period of oil generation [40, 45]. All samples were crushed through 40–60 mesh (0.18–0.25 mm) before the Soxhlet was extracted for 72 h using a solvent mixture of 93% dichloromethane and 7% methanol [13].

The TOC was determined utilizing an Eltra Helios CS elemental analyzer. Before analysis, each shale sample was ground to approximately 100 mesh, and chloroform extraction was performed. Each shale sample (1 g) was mixed with 5% HCl to remove the carbonate component and washed with distilled water. The samples were dried at 70 °C for 12 h before the analysis [30].

Mineralogy compositions of the shale samples were determined via X-ray diffraction (XRD) analysis. Shale block samples were crushed and decomposed, ground with ethanol, and dried at 60 °C, and the final powders were obtained via decanted separation centrifugation. Mineral compositions and relative contents were determined by analyzing 4-μm clay powder using the X-ray diffractometer operating at 104,300 Pa and 18 °C [39]. The mineral composition and respective proportions for each sample were assessed in accordance with the Chinese Oil and Gas Industry Standards SY/T5983-1994 and SY/T5163-1995.

The morphological analysis and microanalysis were conducted via SEM; FEI Quanta 650 FEG). The shale samples were first cut into sheets, and the surface of each sample was then ground and polished via mechanical methods and using argon ions to remove uneven parts and surface attachments before being observed using the SEM.

The morphological analysis and microanalysis were conducted via SEM; FEI Quanta 650 FEG). The shale samples were first cut into sheets, and the surface of each sample was then ground and polished via mechanical methods and using argon ions to remove uneven parts and surface attachments before being observed using the SEM.

The low-pressure CO_2 adsorption and desorption isotherms at different partial pressures were measured at 273 K using a Quantachrome Autosorb-1 sorption analyzer. For the low-pressure N_2 adsorption experiments, an ASAP2020 adsorption instrument was used to measure the N_2 adsorption and desorption isotherms at different partial pressures at 77 K. The adsorption surface was determined using the Brunauer–Emmett–Teller (BET) model, and the pore size distribution (PSD) was calculated using density functional theory (DFT) [28, 30].

3.2 Selection and Definition of Lithofacies Parameters

The classification of shale lithofacies has been extensively studied, considering factors such as clay minerals, felsic minerals, and carbonate minerals. Previous research has employed a ternary classification scheme, dividing shale into argillaceous shale, siliceous shale, carbonate-rich mixed shale (calcareous shale), and mixed shale [18, 22]. However, previous studies have revealed that the Songliao Basin differs from other basins [58]. In the Songliao Basin, the fine-grained sediments primarily comprise clay, and the carbonate content is low, typically existing as a cementation or interlayer [43, 45]. Rock composition cannot adequately distinguish lithofacies types (Fig. 3).

In this study, the division of lacustrine shale lithofacies is no longer confined to rock composition but considers sedimentary structure as the standard to determine the major lithofacies. Changes in sedimentary structure are a direct reflection of the hydrodynamic strength, abundance of material supply, and stability of depositional conditions [25, 59]. We summarized that the laminated forms: wavy laminated, horizontal laminated, and homogeneous laminated.

3.3 Methodology

According to previous studies, the FHH model is more effective and reliable and is widely used in many sedimentary rocks [36, 41]. The FHH model can be expressed as follows:

$$\frac{V}{V_0} = K\left(RTln\left(\frac{P_0}{P}\right)\right)^{-(3-D)} \tag{1}$$

When Eq. (1) is written in log–log terms, we can obtain Eq. (2) as follows:

$$\ln(\mathrm{V}) = (\mathrm{D}-3)\ln\left(\ln\left(\frac{P_0}{P}\right)\right) + C \tag{2}$$

where V is the adsorption volume (cm^3/g) corresponding to the equilibrium pressure P (kPa), K is a constant, R is the universal gas content, T is the absolute temperature, P_0 is the saturation pressure (kPa), C is a constant, and D is the fractal dimension; ln(V) shows a linear relationship with $\ln(\ln(P_0/P))$, and D can be calculated from the slope.

A porous solid has a fractal dimension between 2 and 3 [36]. The closer the fractal dimension to 2, the smoother the shale pore surface, the simpler the pore structure, and the weaker the heterogeneity. The closer the fractal dimension

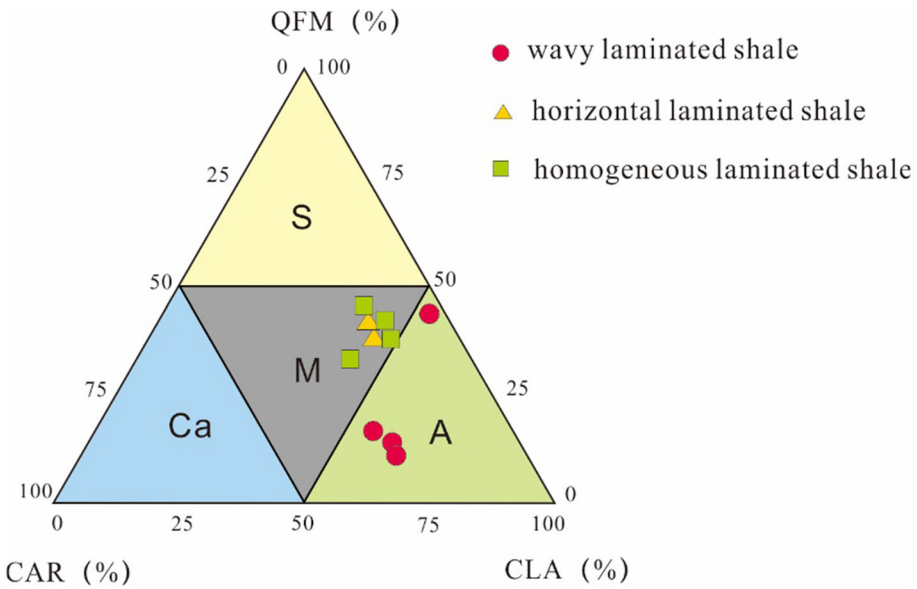

Fig. 3 Ternary diagram showing mineral composition. QFM: brittle minerals such as quartz, feldspar, and mica; CLA: clay; CAR: carbonate

to 3, the rougher the surface, the more complicated the pore structure, and the stronger the heterogeneity [29, 40, 41].

4 Results

4.1 Organic Matter Characteristics and Mineralogical Compositions

The organic matter content of the studied shales varied from 0.62 to 3.51% (avg. 1.59%). Based on TOC content, shales can be named as organic-rich (> 2%), organic-fair (1%–2%), and organic-poor (< 1%) [45, 57], indicating the distribution of organic matter is uneven in Qingshankou. The mineralogical compositions of the shale samples were measured via XRD analysis (Fig. 3a). Clay (avg. 47.01 wt%) and quartz (avg. 28.50 wt%) dominated the mineral components, followed by feldspar (avg. 10.98 wt%), calcite (avg. 7.62 wt%), and pyrite (avg. 2.13 wt%) (Table 1).

4.2 Lithofacies Types and Characteristics

The shale in the Qingshankou member in the central depressed zone of the South Songliao Basin was gray, dark gray, and grayish black. An integration of comprehensive core descriptions and microscopic examinations was derived from 42-m core records; three lithofacies were identified based on sedimentary structure in the Qingshankou shale [60]: wavy laminated shale, horizontal laminated shale, and homogeneous laminated shale.

4.2.1 Wavy Laminated Shale

The mineral composition primarily comprised brittle minerals (40.7–45.1 wt%) and clay minerals less than 50 wt%, of which the quartz content was between 31.8 and 33.6 wt%. The organic matter content of the organic-poor wavy laminated shale was poor, and the TOC value was generally less than 1%, primarily made of light gray bulk fine sandstone, with small amount of mud lamination, carbon, and visible bedding. Under the microscope, dark organic matter and slightly bright silty laminae were observed within the layers (Fig. 4a), with corrugated cross-bedding, parallel bedding (Fig. 4a), and coarse-grade clastic particles. The organic-fair wavy laminated shale, primarily black and gray, had fair organic matter content, generally 1%–2%. Under the microscope, the organic matter mostly occurred in long strips between quartz grains.

4.2.2 Horizontal Laminated Shale

The laminar thickness of horizontal laminated shale was 0.1–1 cm, and mineral composition was dominated by clay minerals (51.6–57.3 wt%, with an average of 54.6 wt%). The TOC value of organic-fair horizontal laminated shale was generally 1%–2%. The color showed gray layer sandwiched with dark gray and black laminated layer (Fig. 4b). Under the microscope, the particle size was very small, relatively dense, and possessed a horizontal microbedding structure, showing the directional arrangement of minerals and organic matter. The organic-rich horizontal laminated shale was mostly pure black, with fine texture, development of laminae, and TOC contents of more than 2%. The dispersed organic matter in the

Table 1 Basic geochemical and mineral compositions of the studied shales

Sample ID	Well	Depth (m)	TOC (%)	Mineralogical composition (wt%)				
				Quartz	Feldspar	Carbonates	Pyrite	Total clays
S1	A	1961.21	0.62	32.3	11.1	5.8	2.0	48.8
S2	A	1980.92	0.76	33.6	11.5	6.6	2.2	46.1
S3	A	1971.49	1.29	31.8	8.9	6.4	3.0	49.9
S4	B	1490.25	1.42	32.8	8.8	6.1	3.2	49.1
S5	B	1501.62	1.93	22.7	8.2	10.4	1.4	57.3
S6	A	1981.12	1.76	29.8	14.1	1.3	1.5	53.3
S7	B	1514.65	2.23	21.3	12.8	12.0	2.3	51.6
S8	B	1517.40	3.51	23.1	8.3	11.3	1.7	55.6
S9	B	1519.17	1.28	29.3	13.4	6.1	2.0	49.2
S10	A	2051.04	1.10	28.3	12.7	10.2	2.0	46.8

organic-rich horizontal laminated shale resulted in a slightly darker matrix.

4.2.3 Homogeneous Laminated Shale

A massive dark gray fabric characterized the homogeneous laminated shale; internal material within beds was relatively uniform, with little variations in composition or texture (Fig. 4c). The organic matter content was relatively high, with an average value of 1%–2%. The mineral composition was dominated by clay minerals of more than 45 wt%. Under the microscope, the mineral distribution of the homogeneous laminated shale samples was relatively uniform, and those samples with a higher TOC had a slightly darker matrix.

4.3 Classification of the Shale Pore System

SEM revealed that pore spaces within the lacustrine shale reservoir of the Qingshankou Formation in the Southern Songliao Basin include mineral interparticle pores, clay mineral intraparticle pores, pyrite intercrystalline pores, mineral dissolution pores, and organic matter pores; there were differences in the types of pores across the different lithofacies.

The wavy laminated shale primarily exhibited interparticle mineral pores and strip-shaped organic matter that developed a small number of original gas pores (Fig. 5a). Many clustered or dispersed framboidal pyrite aggregates were typically associated with organic matter and contained a large number of intercrystalline and interparticle pores (Fig. 5b, c). The horizontal laminated shale primarily contained intraparticle pores within clay minerals and framboidal aggregates, which had diameters of 140–560 nm and comprised multiple pyrite grains (Fig. 5d). Organic matter in the organic-fair horizontal laminated shale was distributed in strips with angular shapes and particle sizes of several to tens of micrometers, and it occupied the interparticle pores of the clay (Fig. 5e). Organic pores developed in the organic-rich horizontal laminated shale (Fig. 5e) were mostly elongated and elliptical and 30–510 nm in size (Fig. 5f). The reservoir pore space of the homogeneous laminated shale was dominated by clay mineral intraparticle pores and interparticle mineral pores. The organic-poor homogeneous laminated shale developed interlayer pores of clay minerals, and the remaining interparticle pores primarily appeared between hard, brittle grains, such as quartz (Fig. 5g). Organic pores were poorly developed and were irregular in shape, with diameters of tens of nanometers (Fig. 5h). Interparticle pores between some clay minerals, brittle minerals, and organic matter were common (Fig. 5i).

4.4 Quantitative Analyses of Pore Structure

4.4.1 Gas Adsorption

CO_2 Adsorption A comparison of the CO_2 adsorption isotherms of the different lithofacies samples is shown in Fig. 6. In all samples, the quantity of adsorbed CO_2 experienced an increase in tandem with the rise in relative pressure. When maintaining identical relative pressure, the amount of gas adsorbed by the horizontal laminated shale was greater than that absorbed by the wavy laminated shale, which in turn was greater than that absorbed by the homogeneous laminated shale. The micropore volumes of wavy laminated shale, horizontal laminated shale, and homogeneous laminated shale were 0.174–0.241 cm^3/100 g, 0.231–0.267 cm^3/100 g, and 0.182–0.203 cm^3/100 g, respectively (Table 2).

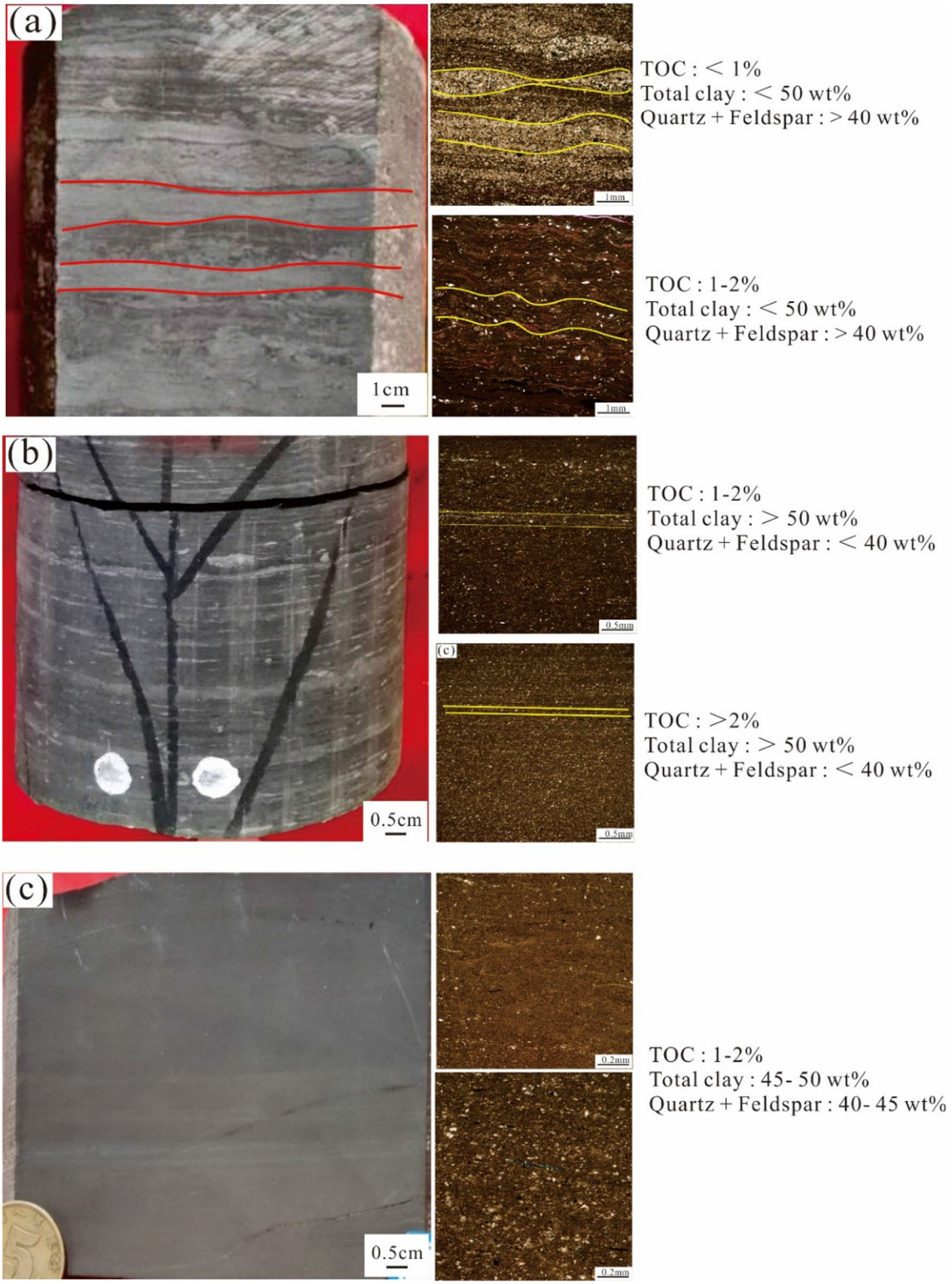

Fig. 4 Lithofacies within the Qingshankou shale. **a** Wavy laminated shale; **b** horizontal laminated shale; and **c** homogeneous laminated shale

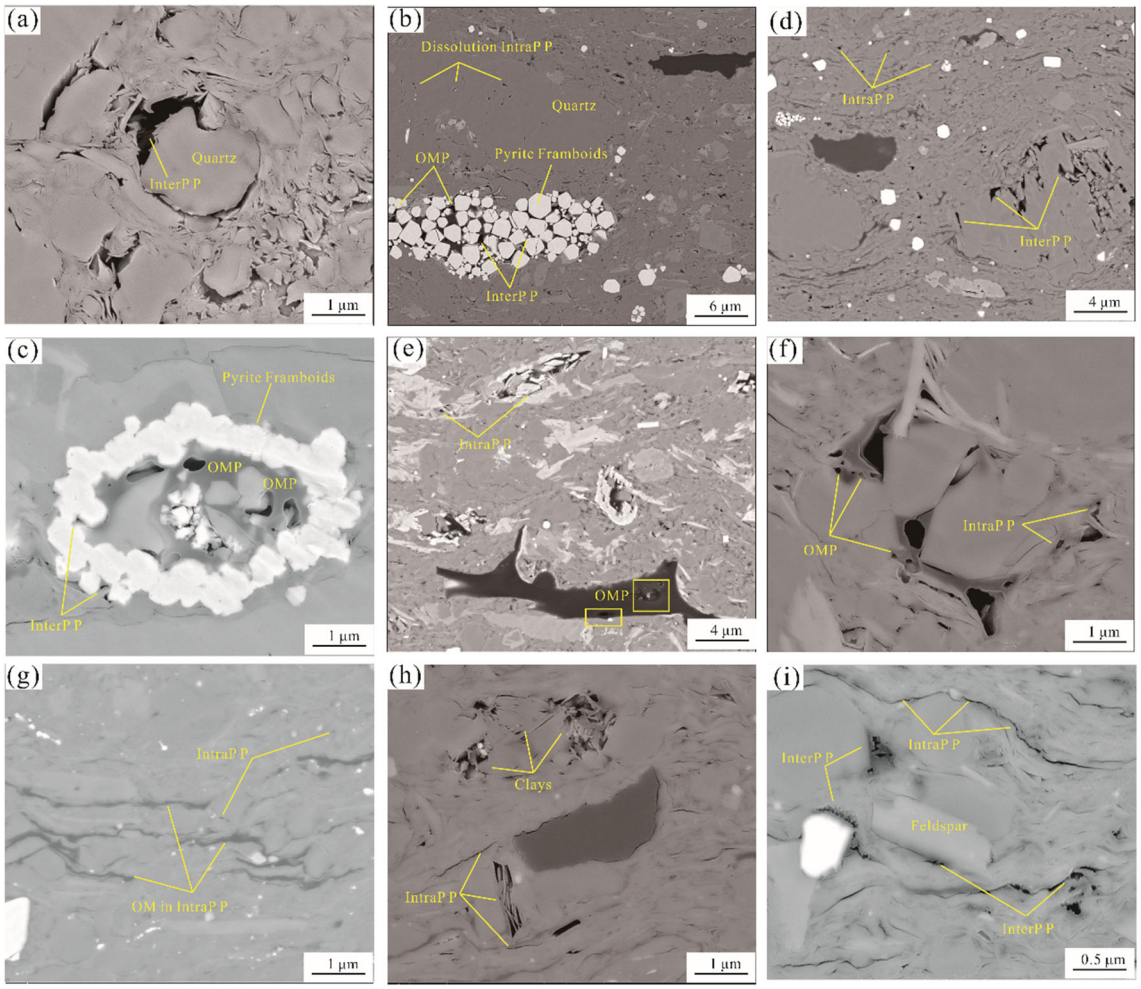

Fig. 5 Scanning electron microscopy images showing the primary pore types in the Qingshankou Member shales: **a** organic matter pores and interparticle pore between quartz mineral particles, S1, organic-poor wavy laminated shale; **b** organic matter occupies the intercrystalline pores associated with pyrite framboids, S3, organic-fair wavy laminated shale; **c** interparticle pores between mineral particles, S4, organic-fair horizontal laminated shale; **d** organic matter occupies the intercrystalline pores associated with pyrite framboids, S3, organic-fair wavy laminated shale; **e** organic matter pores and intraparticle pores within clays, S7, organic-rich horizontal laminated shale; **f** organic matter pores and interparticle pores between minerals, S8, organic-rich horizontal laminated shale; **g** organic matter occupies the intraparticle pores hosted by clays, S9, organic-fair homogeneous laminated shale; **h** organic matter pores and intraparticle pores within clays, S9, organic-fair homogeneous laminated shale; **i** interparticle pore between mineral particles, S10, organic-fair homogeneous laminated shale. OMP: organic matter pores, InterPP: interparticle pores, IntraPP: intraparticle pores

N_2 adsorption The N_2 adsorption isotherms of the shales are shown in Fig. 6. The morphologies of the N_2 adsorption–desorption isotherms of different shale lithofacies were markedly different. According to the IUPAC system [61], the wavy laminated shale hysteresis loop was close to the typical H2 type and has both the characteristic adsorption and desorption curves of the H3 type (Fig. 6a), being horizontal and parallel to each other over a wide pressure range, indicating that this lithofacies is dominated by ink-bottle-shaped macropores [62]. The horizontal laminated shale N_2 adsorption–desorption hysteresis loop was not evident (Fig. 6b). The N_2 adsorption–desorption isotherms of these samples corresponded to type H3 (primarily tabular pores), which is in good correspondence with the abundant tabular pores observed via SEM (Fig. 4d). The homogeneous laminated shale N_2 adsorption–desorption hysteresis loop corresponded to type H4 (Fig. 6c), indicating that the pores of this lithofacies primarily comprised nanopores with a rather irregular (amorphous) structure. These pores are relatively closed and have poor connectivity [62].

The desorption and adsorption curves of all shale samples produced hysteresis loops at $P/P_0 = 0.45$ (Fig. 6). When $P/P_0 < 0.45$, the quantity of adsorbed gas across the different lithofacies was almost identical; however, at $P/P_0 > 0.45$, the hysteresis effect in the wavy laminated shale was more evident than that in the homogeneous laminated shale and

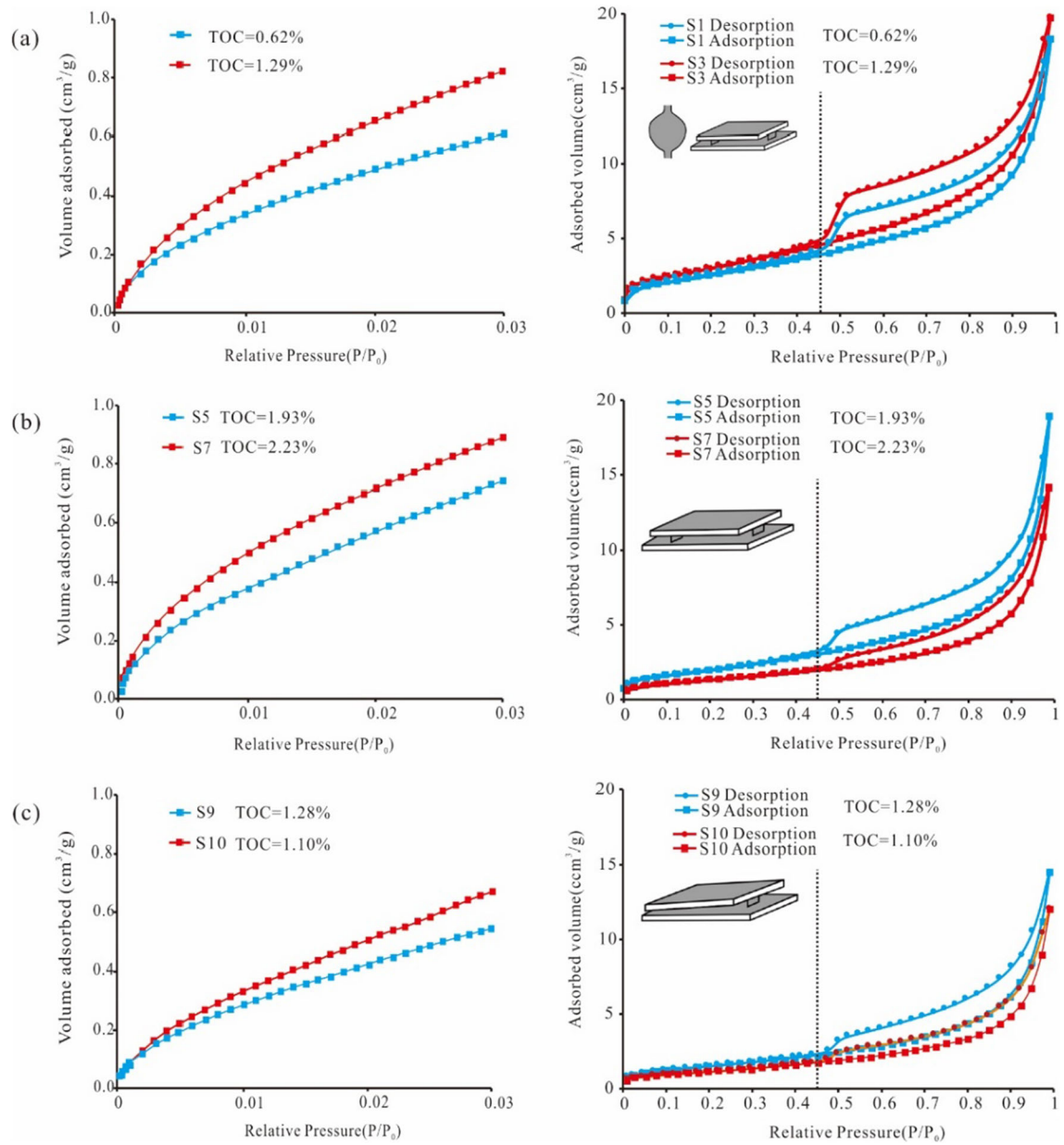

Fig. 6 Comparison of the gas adsorption isotherms from various lithofacies of lacustrine shale: **a** wavy laminated shale; **b** horizontal laminated shale; and **c** homogeneous laminated shale

horizontal laminated shale. This shows that there were more open pores and a certain number of mesopores in the wavy laminated shale.

The mesopore and macropore structural parameters of the different shale lithofacies are presented in Table 2. The DFT pore volume (DFT-PV) of the wavy laminated shale was also higher than that of the horizontal laminated shale. The average pore diameter (APD) of the wavy laminated shale varied from 13.11 to 15.20 nm, whereas those of the homogeneous laminated shale and horizontal laminated shale were 11.87–12.46 nm and 9.23–11.95 nm, respectively.

4.4.2 PSD of Microporosity

The micropore size distribution patterns of the Qingshankou Formation shales, represented by log differential curves concerning pore volume (dV/dlogD), exhibited relatively analogous fluctuation trends (Fig. 7). The PV of the homogeneous laminated shale samples showed a unimodal distribution, with a peak at 0.87 nm and a weak peak widely distributed at 0.50–0.65 nm (Fig. 7). The micropore size distribution curves of the horizontal laminated shale samples showed a

Table 2 Structural parameters of shales obtained via adsorption experiments

Sample ID	Lithofacies	CO_2 adsorption			N_2 adsorption		
		Micropore surface area (m^2/g)	Micropore volume (cm^3/100 g)	DFT pore volume (cm^3/100 g)	Mesopore volume (cm^3/100 g)	Macropore volume (cm^3/100 g)	Average pore diameter (nm)
S1	Organic-poor wavy laminated shale	5.876	0.174	0.521	0.393	0.011	13.20
S2	Organic-poor wavy laminated shale	6.554	0.175	0.441	0.304	0.012	13.11
S3	Organic-fair wavy laminated shale	7.955	0.241	0.400	0.307	0.012	13.41
S4	Organic-fair wavy laminated shale	7.877	0.209	0.512	0.365	0.014	15.20
S5	Organic-fair horizontal laminated shale	8.407	0.249	0.170	0.126	0.007	9.23
S6	Organic-fair horizontal laminated shale	8.345	0.231	0.198	0.143	0.006	9.83
S7	Organic-rich horizontal laminated shale	9.920	0.255	0.211	0.161	0.010	11.95
S8	Organic-rich horizontal laminated shale	10.021	0.267	0.201	0.151	0.009	10.87
S9	Organic-fair homogeneous laminated shale	7.155	0.182	0.312	0.238	0.014	12.46
S10	Organic-fair homogeneous laminated shale	7.982	0.203	0.322	0.234	0.021	11.87

distinct peak at approximately 0.82 nm in diameter and developed at approximately 0.75–0.85 nm in diameter (Fig. 7b). The micropore size distribution curves of the wavy laminated shale samples showed a conspicuous single peak at approximately 0.90 nm in diameter and two weak peaks at 0.42–0.60 nm and 0.65–0.72 nm (Fig. 7c). The shale PSD showed that the micropore size was dominated by pores with diameters of < 1.0 nm. Compared with those of the wavy laminated shale and homogeneous laminated shale, the micropore size (0.75–0.85 nm) of the horizontal laminated shale contributed to a greater extent to the total volume.

The mesopore and macropore size distribution curves of the three lithofacies, obtained via N_2 adsorption experiments, are shown in Fig. 7. Mesopores with pore diameters of 1 nm and 4–10 nm markedly contributed to the PV in the wavy laminated shale, showing a double-peak characteristic (Fig. 7a).

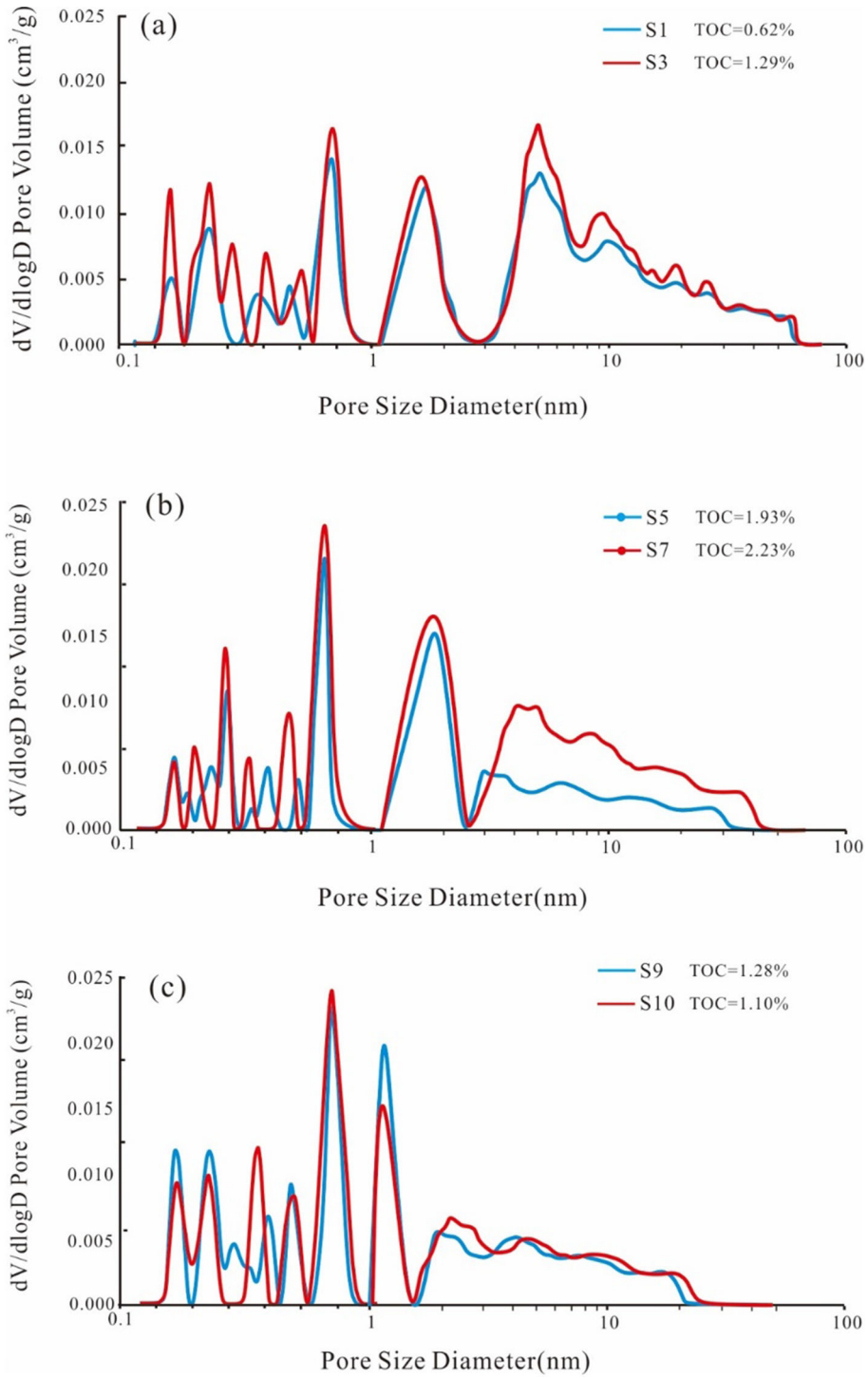

Fig. 7 Micropore size distributions for various lithofacies of lacustrine shale: **a** wavy laminated shale; **b** horizontal laminated shale; and **c** homogeneous laminated shale

Contributions to the PV of the horizontal laminated shale primarily originated from pores of 1–2 nm and 3–5 nm, and all samples showed a double peak, with TOC content having a substantial influence on both PV (Fig. 7b). However, the small pore size mesopores of the homogeneous laminated shale, concentrated in the size ranges of 1–1.5 nm and 2–4 nm, markedly contributed to the PV (Fig. 7c).

4.5 Fractal Characteristics

Figure 8 shows the plots of lnV versus $\ln(\ln(P_0/P))$ for the different lithofacies, which appear as two distinct linear regions. This indicates a gas adsorption mechanism and fractal features within these two intervals [6]. Therefore, when calculating the fractal dimensions, two fractal dimensions,

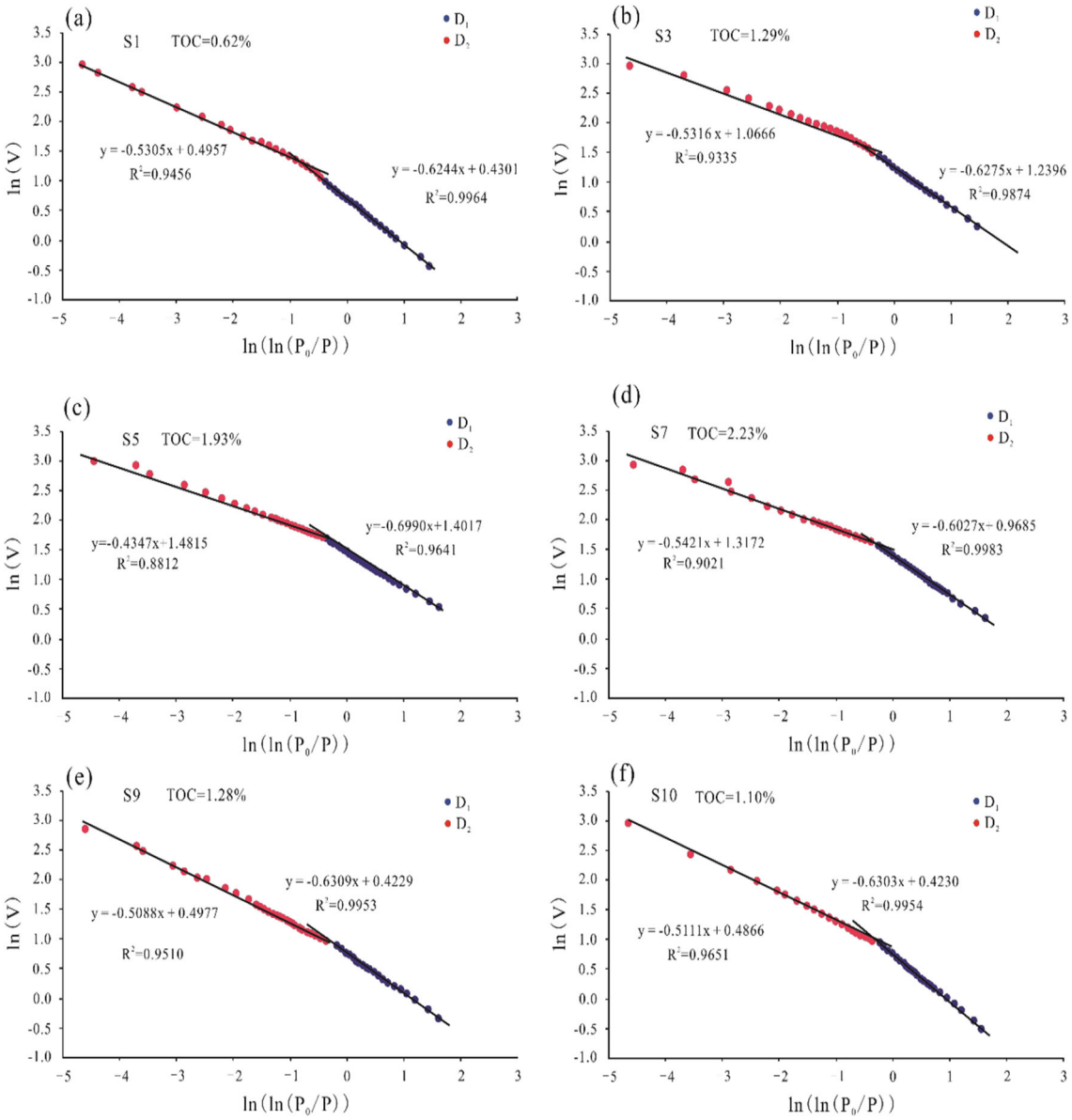

Fig. 8 Plots of ln V versus ln(ln(P_0/P)) for various lithofacies of lacustrine shale

D_1 and D_2, were generated. According to the DFT theoretical equation, D_1 corresponds to the low-pressure region (P/P_0 < 0.45), where nitrogen is primarily adsorbed on the monolayer or multi-molecular layer of the shale pore surface; this reflects the complexity of the shale pore surface morphology [35, 37]. D_2 corresponds to the high-pressure zone (P/P_0 > 0.45), which primarily undergoes capillary condensation and reflects the complexity of the shale microscopic pore structure [34, 36, 37].

The results of the D_1 and D_2 linear regression analyses are presented in Table 3. The D_1 values ranged from 2.3010 to 2.3973, and the D_2 values ranged from 2.4606 to 2.5653. The D_1 values of all lithofacies types were smaller than the D_2 values, indicating that the shale pore structure was more complex and heterogeneous than the specific surface area. The D_1 values of the wavy laminated shale ranged from 2.3711 to 2.3756, whereas those of the homogeneous laminated shale ranged between 2.3691 and 2.3697. The D_1 values of horizontal laminated shale greatly varied, from 2.3010 to 2.3973, showing that its pore surface area morphology was complex. The D_2 values of the wavy laminated shale (2.4606–2.4702) were relatively small, and the D_2 values of the organic-rich horizontal laminated shale (2.4579–2.4607) were smaller than that of the organic-fair horizontal laminated shale (2.5653–2.4944), showing that

Table 3 Fractal dimensions (D_1 and D_2) of the three lithofacies. R^2 = fitting coefficient

Sample ID	Lithofacies	Fractal dimension					
		D_1 fitting equation	R^2	D_1	D_2 fitting equation	R^2	D_2
S1	Organic-poor wavy laminated shale	$y = -0.6244x + 0.4301$	0.9964	2.3756	$y = -0.5305x + 0.4957$	0.9456	2.4695
S2	Organic-poor wavy laminated shale	$y = -0.6268x + 0.4302$	0.9948	2.3732	$y = -0.5298x + 0.4888$	0.9665	2.4702
S3	Organic-fair wavy laminated shale	$y = -0.6275x + 1.2396$	0.9874	2.3725	$y = -0.5316\ x + 1.0666$	0.9335	2.4684
S4	Organic-fair wavy laminated shale	$y = -0.6289x + 0.5509$	0.9918	2.3711	$y = -0.5394\ x + 1.0547$	0.9266	2.4606
S5	Organic-fair horizontal laminated shale	$y = -0.6990x + 1.4017$	0.9641	2.3010	$y = -0.4347x + 1.4815$	0.8812	2.5653
S6	Organic-fair horizontal laminated shale	$y = -0.6352x + 0.675$	0.9919	2.3648	$y = -0.5056x + 0.7691$	0.9310	2.4944
S7	Organic-rich horizontal laminated shale	$y = -0.6027x + 0.9685$	0.9983	2.3973	$y = -0.5421x + 1.3172$	0.9021	2.4579
S8	Organic-rich horizontal laminated shale	$y = -0.6121x + 0.9597$	0.9979	2.3879	$y = -0.5393x + 0.6197$	0.9542	2.4607
S9	Organic-fair homogeneous laminated shale	$y = -0.6309x + 0.4229$	0.9953	2.3691	$y = -0.5088x + 0.4977$	0.951	2.4912
S10	Organic-fair homogeneous laminated shale	$y = -0.6303x + 0.4230$	0.9954	2.3697	$y = -0.5111x + 0.4866$	0.9651	2.4889

the wavy laminated shale and organic-rich horizontal laminated shale have a relatively simple pore structure and low heterogeneity.

5 Discussion

5.1 Difference in pore structures

The PSD in organic shale spanned a broad spectrum, covering nano- to micrometer scales. The pore structure analysis derived from N_2 adsorption exposed pore dimensions ranging from 1.2 to 100 nm, with Fig. 9 demonstrating the contributions of varying scales to the pore volume (PV). The pore size distribution displays a multi-peak pattern, with mesopores contributing to approximately 57% of the total pore volume, micropores contributing to about 31%, and macropores accounting for a small portion of the total pore volume. The wavy laminated shale had a high volume fraction of mesopores (58.76%–62.41%), with a reduced contribution from micropores and macropores. In contrast, the pore volume of the horizontal laminated shale was dominated by micropores, which accounted for 51.10%–59.21% of the total pore volume, followed by mesopores. Homogeneous laminated shale micropores contributed more to the total pore volume, with an average of 61.62%. Both micropores and mesopores were plentiful in all shale samples, representing over 90% of the cumulative pore volume, underscoring the importance of these pore types in shale reservoirs.

Unlike horizontal laminated shale and homogeneous laminated shale, wavy laminated shale was dominated by pore diameter of 2–50 nm (Fig. 9a), and the organic matter pores were relatively poor and isolated (Fig. 5a). The different pore diameters of the wavy laminated shale were less affected by TOC content (Fig. 9a), indicating that these lithofacies primarily contained inorganic pores. In addition, with the increase in TOC content, the proportion of pores with diameter < 2 nm increased, and the proportion of pores with diameter 2–50 nm decreased (Fig. 9b). During burial, organic matter is prone to intense extrusion, leading to changes in pore diameter. The pores of mesopores or macropores shrank into micropores, thereby reducing the variations in the APD of organic matter (Fig. 5f).

5.2 Factors Controlling the Pore Structures

The Qingshankou Formation shale exhibited a complex pore network based on N_2 PSD (Fig. 7). Fractal dimensions should be calculated to characterize the complexity of pore structure in oil shales and analyze the factors controlling the pore structure of distinct lithofacies.

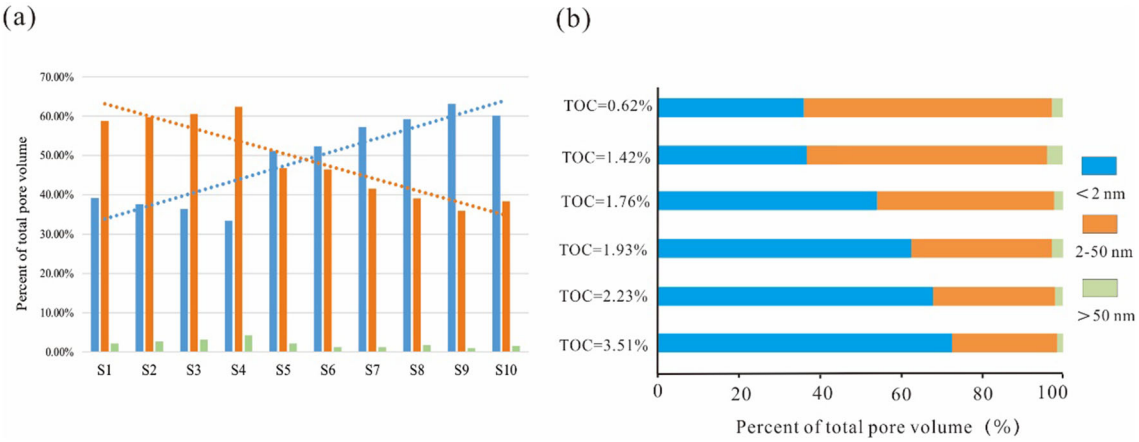

Fig. 9 Percentage of pores with different diameter ranges based on N_2 adsorption data. **a** Percentage of pores with different diameter ranges with lithofacies. **b** Percentage of pores with different diameter ranges with increasing TOC content

5.2.1 Relationships Between Fractal Dimensions and Pore Structure Parameters

The relationships between the fractal dimensions and pore structure parameters showed that relationships of the two fractal dimensions with the DFT pore volume are similar to those with the APD, exhibiting a strong correlation with horizontal laminated shales (Fig. 10). Variations in correlations between fractal dimensions (D_1 and D_2) and DFT pore volume areas might be associated with the relative pressure ranges for calculating D_1 and D_2, which span from 0 to 0.45 and from 0.45 to 1.0, respectively [28, 63]. In accordance with the Kelvin equation, smaller pores were filled with nitrogen at P/Po > 0.45 compared to those at P/Po < 0.45. Therefore, D_1 reflects smaller pore volume and pore size characteristics than D_2. The correlation between horizontal laminated shales and DFT pore volume was better than that between wavy laminated shales and DFT pore volume. This may be because horizontal laminated shales were primarily micropores, which contribute more to DFT pore volume than mesopore (Fig. 9a and 10b). Our analysis revealed that the large average pore size of horizontal laminated shale favors the seepage and production of shale oil.

5.2.2 Relationships Between Fractal Dimensions and Mineral Content

The correlations between the fractal dimensions (D_1 and D_2) and the quartz, pyrite, and clay contents of each lithofacies were analyzed (Fig. 11). Fractal dimension D_1 of wavy laminated shale showed a strong positive correlation with quartz mineral content, whereas that of horizontal laminated shale showed no evident relationship with quartz mineral content (Fig. 11a). The variation in fractal dimension among distinct lithofacies might be linked to the quartz origin. Wavy laminated shales contained substantial amounts of authigenic quartz, generally consisting of small quartz crystal grains. The dimensions of these euhedral quartz particles ranged from nanoscale to 3 μm, and they were in close contact with organic matter, with some even encircled by it (Fig. 5a). The presence of authigenic quartz markedly increases rough surface of quartz and reduces PSD [64]. Fractal dimension D_1 of horizontal laminated shales was weakly positively correlated with pyrite content (Fig. 11b). The intercrystalline organic matter nanopores of the framboidal pyrite aggregate were intensively developed in the interparticle organic matter, forming a honeycomb organic matter pore network (Fig. 5d). The framboidal pyrite aggregate had large intergranular pore surface area and good connectivity, which are conducive to the desorption, diffusion, and seepage of shale oil [65]. Therefore, the higher the pyrite content, the larger the D_1; however, the relationship between D_2 and the pyrite content was not evident (Fig. 11b), indicating that the pyrite content had little effect on the heterogeneity of the pore structure.

In addition, clay minerals had a remarkable influence on both pore surface area and pore structure; however, the influence on pore structure of distinct lithofacies was opposite (Fig. 11c). In the horizontal laminated shale rich in clay minerals and organic matter, the clay minerals reduced the complexity of pore structure. The clay minerals in horizontal laminated shales comprised different kinds of minerals, which may contain different types and scales of pores (Fig. 5d, e). Another key controlling factor may be that organic matter distributed in strips was surrounded by clay minerals (Fig. 5e). Clay minerals are the "mystery" of long-term preservation of organic matter in sediments [53]; however, more persuasive data are required to substantiate this.

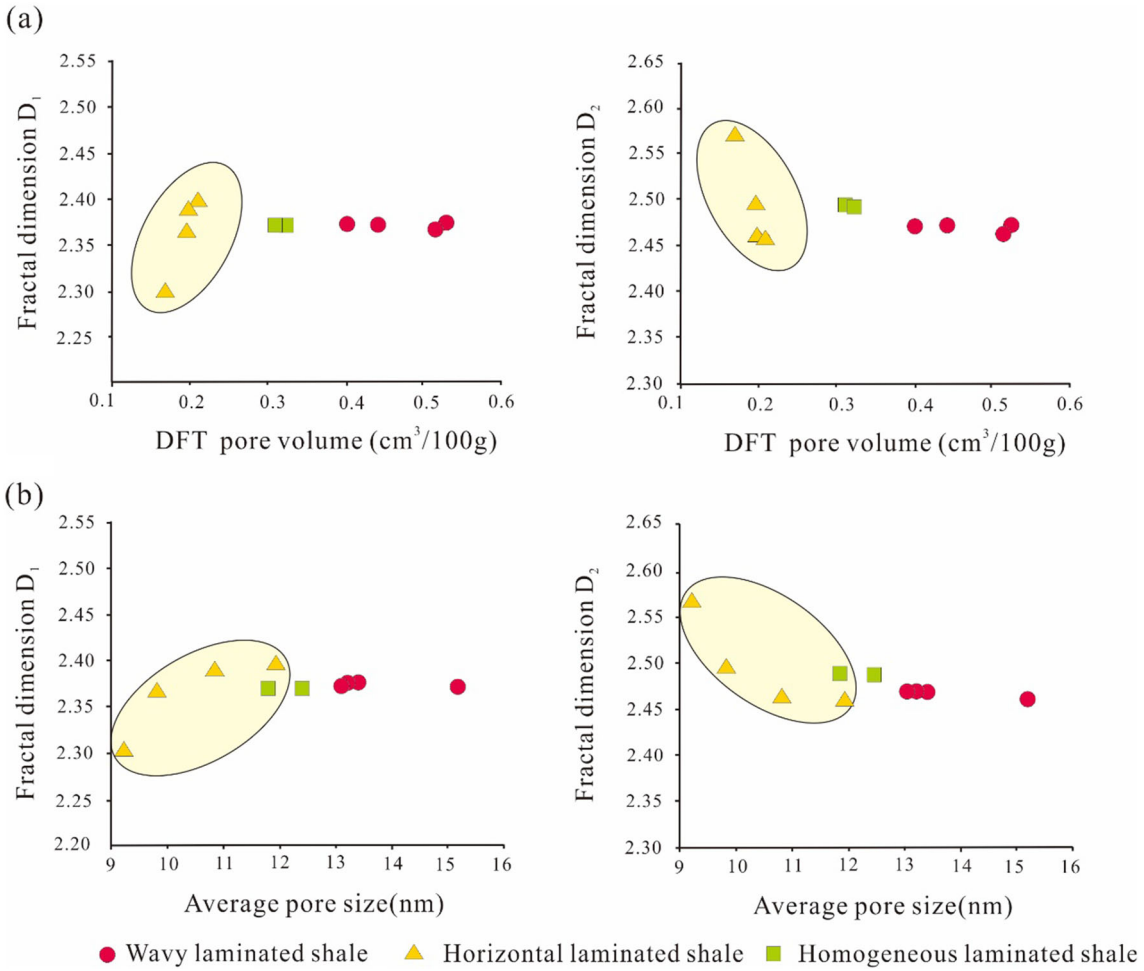

Fig. 10 Relationships between fractal dimensions and pore structure parameters: **a** DFT pore volume and **b** average pore diameter

5.3 Implications of Sedimentary Environment for the Pore Structures

5.3.1 Sedimentary Environment with the Development of Distinct Lithofacies

The sedimentary environment determines the material composition and structure of shale lithofacies [25, 57, 66]. During the sedimentary period of Qingshankou Formation in Songliao Basin, large-scale water inflow occurred, forming a large and wide depression lake basin with water depth of semi-deep lake to deep lake [44, 57]. Previous studies have suggested that sedimentary facies and their sedimentary characteristics can be identified from Qingshankou core descriptions of lithofacies to build a shallow lacustrine and semi-deep to deep lacustrine facies [44, 57]. The wavy laminated shale, characterized by the presence of sandstone and siltstone layers that are thin and discontinuous (Fig. 4a), is interpreted to have formed in the outer front of the delta or shallow lacustrine environment. This lithofacies results from mechanical transport deposition and chemical deposition under relatively unstable water conditions, increased terrigenous sources, brackish water, and a reducing environment [57, 67, 68]. On the other hand, the horizontal laminated shale is primarily developed in the semi-deep lake to deep lake facies. It is associated with seasonal changes in salinized quiet water and a reducing environment [19, 57]. Finally, the homogeneous laminated shale is predominantly found in the shore-shallow lake facies, representing a deep-water subtidal zone characterized by low-energy sedimentation linked to transgression [59, 69]. The succession of wavy laminated shale, homogeneous laminated shale, and horizontal laminated shale from the basin margin to the subsag in the Qingshankou Formation of the Southern Songliao Basin is in agreement with the established models of shale deposition (Fig. 12). In addition, our model depicting the succession of wavy laminated shale, homogeneous laminated shale, and horizontal laminated shale in the Qingshankou Formation of the Southern Songliao Basin is consistent with the shale deposition models identified worldwide [60, 70]. Based on

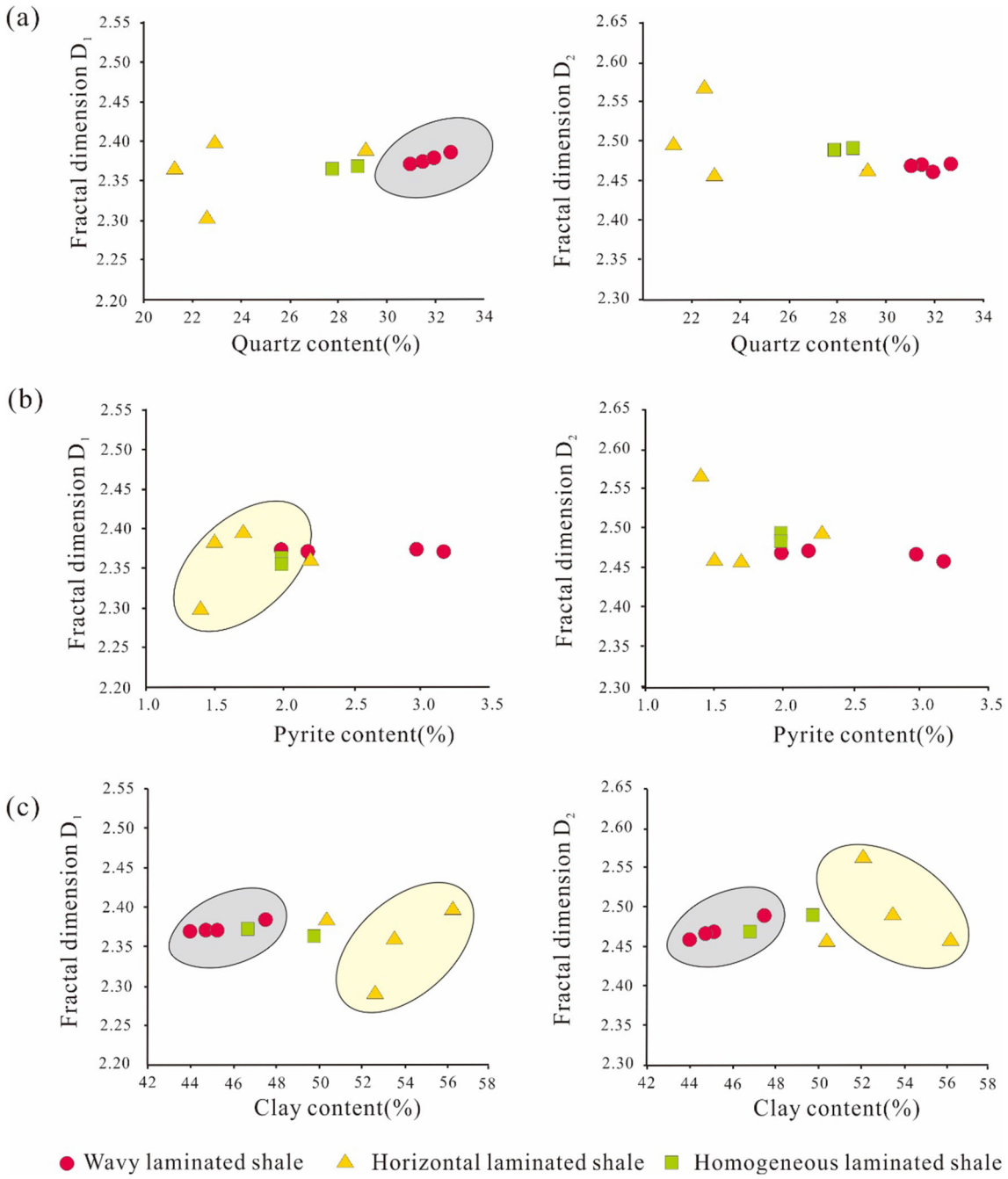

Fig. 11 Relationships between fractal dimensions and mineral contents: **a** quartz content; **b** pyrite content; and **c** clay content

extensive research in various shale reservoirs, these models have provided valuable insights into the depositional processes and environments associated with different lithofacies. Our findings further support the validity and applicability of these established shale deposition models, reinforcing the understanding of shale reservoir development and characterization.

5.3.2 Geological Significance of Pore Structures

The wavy laminated shale is abundant in the delta front, where the lake surface is shallow formed in the presence of abundant detrital input, with giant grain size and low clay content [21, 68] (Fig. 12a). The detrital rigid grains are likely to be stacked into a rigid framework, which is more favorable for the preservation of inorganic pores than that of other

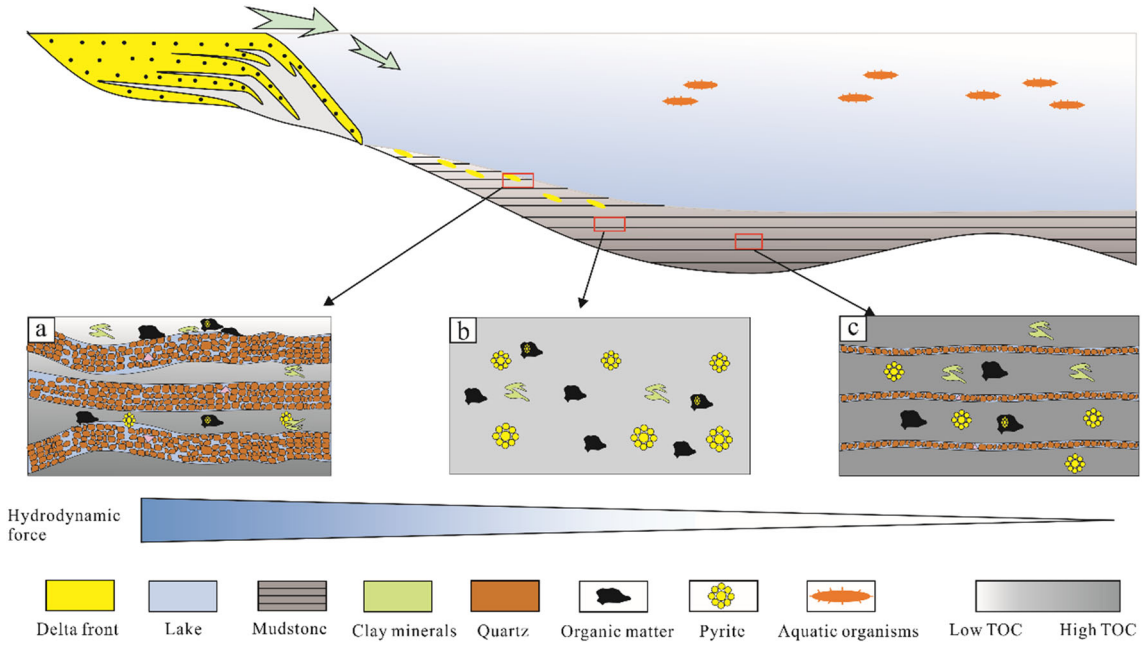

Fig. 12 Conceptual model showing microscopic mineral content related to sedimentary pattern of lacustrine shale: **a** wavy laminated shale; **b** homogeneous laminated shale; and **c** horizontal laminated shale

lithofacies in shale. In shore-shallow lake facies, the homogeneous laminated shale constantly subsided and accumulated, forming a relatively closed fluid environment [69], resulting in relatively closed pores and poor connectivity (Fig. 12b). The horizontal laminated shale was primarily formed in a semi-deep lake-deep lake environment, and the sedimentary structure is primarily horizontal laminae. The water is calm, and the hydrodynamic condition is weak during the sedimentary period. In the horizontal laminated shale, massive input of terrigenous clasts was not as well developed as in wavy laminated shale (Fig. 12c). However, parallel bedding develops with the fluctuations in lake level, forming a relatively open fluid environment [71]. Furthermore, minimal detrital input in oxygen- and nutrient-rich shallow waters under a semihumid to humid climate promotes an increase in TOC abundance [57]. High-quality reservoirs are preserved within organic pores featuring a large specific surface area. Consequently, the wavy laminated shale and organic-rich horizontal laminated shale in the Qingshankou Formation's lacustrine shale constitute ideal source-reservoir unit systems for petroleum generation, migration, and accumulation.

6 Conclusions

(1) In the Qingshankou Formation lacustrine shale, three lithofacies were discerned based on sedimentary structures: wavy laminated shale, horizontal laminated shale, and homogeneous laminated shale. These lithofacies significantly influenced pore types and pore structures related to oil storage. The wavy laminated shale exhibited numerous interparticle and intraparticle pores, displaying pore diameters of 2-50 nm, resulting from dissolution-related pores in brittle minerals, effectively expanding oil storage capacity. In contrast, horizontal laminated shale and homogeneous laminated shale predominantly featured micropores, which were substantially affected by TOC.

(2) The shale pore structure exhibited greater complexity and heterogeneity than the pore surface roughness when integrating fractal theory with N2 adsorption tests. In wavy laminated shale, quartz and clay minerals directly impacted the pore structure and pore diameter variability. The irregularity of pore surfaces in horizontal laminated shale and homogeneous laminated shale was similar.

(3) The wavy laminated shale and organic-rich horizontal laminated shale within the Qingshankou Formation lacustrine shale can therefore be regarded as ideal source-reservoir unit systems for petroleum generation, migration, and accumulation. Horizontal laminated shale led to the formation of oxygen-depleted sedimentary water, which in turn resulted in relatively closed pores and limited connectivity.

Acknowledgements This research was co-funded by "the National Key Research and Development Programs of China (Nos.2018YFC0604304, 2017YFC603104)." We express our gratitude to the geologists at the Exploration and Development Research Institute of Jilin Oilfield Company, CNPC, for granting us permission to utilize the geological data in this study.

References

1. Zou, C.N.; Yang, Z.; Cui, J.W.; Zhu, R.K.; Hou, L.H.; Tao, S.Z.; Yuan, X.J.; Wu, S.T.; Lin, S.; Wang, L.: Formation mechanism, geological characteristics and development strategy of nonmarine shale oil in China. Petroleum Explor. Develop. **40**, 15–27 (2013)
2. Gou, Q.Y.; Xu, S.; Hao, F.; Shu, Z.G.; He, S.; Wu, Z.R.: Differences in the nanopore structure of organic-rich shales with distinct sedimentary environments and mineral compositions. Energy & Fuels. **35**, 16562–16577 (2021)
3. Zhu, X.M.; Zhang, M.Z.; Zhu, S.F.; Dong, Y.L.; Li, C.; Bi, Y.Q.; Ma, L.: Shale Lithofacies and Sedimentary Environment of the Third Member, Shahejie Formation, Zhanhua Sag, Eastern China. Acta Geologica Sinica - English Edition. **96**, 1024–1040 (2022)
4. Zhang, J.; Jia, Y.; Du, G.: Diagenesis and its effect on reservoir quality of Silurian sandstones, Tabei area, Tarim Basin China. Petroleum Sci. **4**, 1–13 (2007)
5. Han, H.; Guo, C.; Zhong, N.; Pang, P.; Gao, Y.: A study on fractal characteristics of lacustrine shales of Qingshankou Formation in the Songliao Basin, northeast China using nitrogen adsorption and mercury injection methods. J. Petrol. Sci. Eng. **193**, (2020)
6. Wang, Y.; Liu, L.; Cheng, H.: Gas adsorption characterization of pore structure of organic-rich shale: insights into contribution of organic matter to shale pore network. Natural Resour. Res. **30**, 2377–2395 (2021)
7. Li, Y.; Chen, J.; Elsworth, D.; Pan, Z.; Ma, X.: Nanoscale mechanical property variations concerning mineral composition and contact of marine shale. Geosci. Front. **13**, 4 (2022)
8. Ross, D.J.; Bustin, R.M.: The importance of shale composition and pore structure upon gas storage potential of shale gas reservoirs. Marine and Petroleum Geol. **26**, 916–927 (2009)
9. Loucks, R.G.; Reed, R.M.; Ruppel, S.C.; Hammes, U.: Spectrum of pore types and networks in mudrocks and a descriptive classification for matrix-related mudrock pores. AAPG Bull. **96**, 1071–1098 (2012)
10. Liu, K.Q.; Ostadhassan, M.; Zhou, J.; Gentzis, T.; Rezaee, R.: Nanoscale pore structure characterization of the Bakken shale in the USA. Fuel **209**, 567–578 (2017)
11. Cockreham, C.B.; Zhang, X.; Lau, M.L.; Long, M.; Guo, X.; Xu, H.; Wu, D.: Thermal evolutions and resulting microstructural changes in kerogen-rich marcellus shale. ACS Earth and Space Chem. **4**, 2461–2469 (2020)
12. Xu, Y.; Lun, Z.; Pan, Z.; Wang, H.; Zhou, X.; Zhao, C.; Zhang, D.: Occurrence space and state of shale oil: a review. J. Petroleum Sci. Eng. **211**, (2022)
13. Wang, M.; Ma, R.; Li, J.B.; Lu, S.F.; Li, C.; Guo, Z.; Li, Z.: Occurrence mechanism of lacustrine shale oil in the Paleogene Shahejie Formation of Jiyang depression, Bohai Bay Basin China. Petroleum Explor. Develop. **46**, 833–846 (2019)
14. Slatt, R.M.; O'Brien, N.R.: Pore types in the Barnett and Woodford gas shales: Contribution to understanding gas storage and migration pathways in fine-grained rocks. AAPG Bull. **95**, 2017–2030 (2011)
15. Chalmers, G.R.; Bustin, R.M.; Power, I.M.: Characterization of gas shale pore systems by porosimetry, pycnometry, surface area, and field emission scanning electron microscopy/transmission electron microscopy image analyses Examples from the Barnett, Woodford, Haynesville, Marcellus, and Doig units. AAPG Bull. **96**, 1099–1119 (2012)
16. Curtis, M.E.; Cardott, B.J.; Sondergeld, C.H.; Rai, C.S.: Development of organic porosity in the Woodford Shale with increasing thermal maturity. Int. J. Coal Geol. **103**, 26–31 (2012)
17. Wang, R.Y.; Ding, W.L.; Zhang, Y.Q.; Wang, Z.; Wang, X.; He, J.; Zeng, W.; Dai, P.: Analysis of developmental characteristics and dominant factors of fractures in Lower Cambrian marine shale reservoirs: a case study of Niutitang formation in Cen'gong block, southern China. J. Petrol. Sci. Eng. **138**, 31–49 (2016)
18. Lazar, O.R.; Bohacs, K.M.; Macquaker, J.H.; Schieber, J.; Demko, T.M.: Capturing key attributes of fine-grained sedimentary rocks in outcrops, cores, and thin sections: nomenclature and description guidelines. J. Sedimentary Res. **85**, 230–246 (2015)
19. Tang, X.; Jiang, Z.; Huang, H.; Jiang, S.; Yang, L.; Xiong, F.; Chen, L.; Feng, J.: Lithofacies characteristics and its effect on gas storage of the Silurian Longmaxi marine shale in the southeast Sichuan Basin, China. J. Natural Gas Sci. Eng. **28**, 338–346 (2016)
20. Yang, G.; Zeng, J.; Qiao, J.; Liu, Y.; Cao, W.; Wang, C.; Geng, F.; Wei, W.: Differences between laminated and massive shales in the permian lucaogou formation: Insights into the Paleoenvironment, Petrology, Organic Matter, and Microstructure. ACS Earth and Space Chem. **6**, 2530–2551 (2022)
21. Peng, J.; Milliken, K.L.; Fu, Q.; Janson, X.; Hamlin, H.S.: Grain assemblages and diagenesis in organic-rich mudrocks, Upper Pennsylvanian Cline shale (Wolfcamp D), Midland Basin. Texas. AAPG Bull. **104**, 1593–1624 (2020)
22. Milliken, K.: A compositional classification for grain assemblages in fine-grained sediments and sedimentary rocks. J. Sedimentary Res. **84**, 1185–1199 (2014)
23. Schieber, J.: Early diagenetic silica deposition in algal cysts and spores; a source of sand in black shales? J. Sedimentary Res. **66**, 175–183 (1996)
24. Chalmers, G.R.; Bustin, R.M.; Power, I.M.J.A.: Characterization of gas shale pore systems by porosimetry, pycnometry, surface area, and field emission scanning electron microscopy/transmission electron microscopy image analyses: Examples from the Barnett, Woodford, Haynesville, Marcellus, and Doig units Characterization of Gas Shale Pore Systems. AAPG Bull. **96**, 1099–1119 (2012)
25. Ringrose, P.; Sorbie, K.; Corbett, P.; Jensen, J.: Immiscible flow behaviour in laminated and cross-bedded sandstones. J. Petroleum Sci. Eng. **9**, 103–124 (1993)
26. Klaver, J.; Desbois, G.; Littke, R.; Urai, J.L.: BIB-SEM characterization of pore space morphology and distribution in postmature to overmature samples from the Haynesville and Bossier Shales. Mar. Pet. Geol. **59**, 451–466 (2015)
27. Wang, P.; Jiang, Z.; Ji, W.; Zhang, C.; Yuan, Y.; Chen, L.; Yin, L.: Heterogeneity of intergranular, intraparticle and organic pores in Longmaxi shale in Sichuan Basin, South China: Evidence from SEM digital images and fractal and multifractal geometries. Mar. Pet. Geol. **72**, 122–138 (2016)
28. Li, Y.; Wang, Z.; Pan, Z.; Niu, X.; Yu, Y.; Meng, S.: Pore structure and its fractal dimensions of transitional shale: a cross-section from east margin of the Ordos Basin. China. Fuel. **241**, 417–431 (2019)
29. Wu, Y.; Liu, C.; Ouyang, S.; Luo, B.; Zhao, D.; Sun, W.; Awan, R.; Lu, Z.; Li, G.; Zang, Q.: Investigation of pore-throat structure and fractal characteristics of tight sandstones using HPMI, CRMI, and NMR methods: a case study of the lower Shihezi formation in the Sulige area, Ordos Basin. J. Petroleum Sci. Eng. **210**, 110053 (2022)
30. Zhou, Q.; Zhang, D.; Li, X.; Qian, Z.; Chen, G.; Lyu, C.; Ma, X.; Li, C.: Insight into the desorption behavior and mechanism of tight oil with in-situ low-temperature thermal. J. Petroleum Sci. Eng. **218**, 111001 (2022)
31. Gou, Q.; Xu, S.; Hao, F.; Yang, F.; Zhang, B.; Shu, Z.; Zhang, A.; Wang, Y.; Lu, Y.; Cheng, X.: Full-scale pores and microfractures characterization using FE-SEM, gas adsorption, nano-CT and micro-CT: a case study of the Silurian Longmaxi Formation shale in the Fuling area, Sichuan Basin. China. Fuel. **253**, 167–179 (2019)
32. Zhao, R.; Xue, H.; Lu, S.; Li, J.; Tian, S.; Wang, M.; Dong, Z.: Multi-scale pore structure characterization of lacustrine shale and its coupling relationship with material composition: an integrated

study of multiple experiments. Marine and Petroleum Geol. **140**, 105648 (2022)
33. Wang, M.; Xue, H.; Tian, S.; Wilkins, R.W.T.; Wang, Z.: Fractal characteristics of Upper Cretaceous lacustrine shale from the Songliao Basin NE China. Marine and Petroleum Geol. **67**, 144–153 (2015)
34. Li, A.; Ding, W.; He, J.; Dai, P.; Yin, S.; Xie, F.: Investigation of pore structure and fractal characteristics of organic-rich shale reservoirs: a case study of Lower Cambrian Qiongzhusi formation in Malong block of eastern Yunnan Province. South China. Marine and Petroleum Geol. **70**, 46–57 (2016)
35. Yang, C.; Zhang, J.; Wang, X.; Tang, X.; Chen, Y.; Jiang, L.; Gong, X.: Nanoscale pore structure and fractal characteristics of a marine-continental transitional shale: a case study from the lower Permian Shanxi Shale in the southeastern Ordos Basin China. Marine and Petroleum Geol. **88**, 54–68 (2017)
36. Mishra, D.K.; Samad, S.K.; Varma, A.K.; Mendhe, V.A.: Pore geometrical complexity and fractal facets of Permian shales and coals from Auranga Basin, Jharkhand, India. J. Petrol. Sci. Eng. **52**, 25–43 (2018)
37. Wang, X.; Hou, J.; Li, S.; Dou, L.; Song, S.; Kang, Q.; Wang, D.: Insight into the nanoscale pore structure of organic-rich shales in the Bakken Formation, USA. J. Petroleum Sci. Eng. **191**, 107182 (2020)
38. Jiang, F.; Chen, D.; Chen, J.; Li, Q.; Dai, J.: Fractal analysis of shale pore structure of continental shale gas reservoir in the Ordos Basin NW China. Energy & Fuels. **30**, 6 (2016)
39. Wang, Y.; Cheng, H.; Hu, Q.; Liu, L.; Jia, L.; Gao, S.; Wang, Y.: Pore structure heterogeneity of Wufeng-Longmaxi shale, Sichuan Basin, China: Evidence from gas physisorption and multifractal geometries. J. Petroleum Sci. Eng. **208**, 109313 (2022)
40. Han, H.; Guo, C.; Zhong, N.; Pang, P.; Gao, Y.: A study on fractal characteristics of lacustrine shales of Qingshankou Formation in the Songliao Basin, northeast China using nitrogen adsorption and mercury injection methods. J. Petroleum Sci. Eng. **193**, 107378 (2020)
41. Turlapati, V.Y.; Prusty, B.K.; Bakshi, T.: Detailed pore structure study of damodar valley and upper assam basin shales using fractal analysis. Energy & Fuels. **34**, 14001–14011 (2020)
42. Dong, T.; He, S.; Wang, D.; Hou, Y.: Hydrocarbon migration and accumulation in the Upper Cretaceous Qingshankou formation, Changling Sag, southern Songliao Basin: Insights from integrated analyses of fluid inclusion, oil source correlation and basin modelling. J. Asian Earth Sci. **90**, 77–87 (2014)
43. Liu, B.; Lu, Y.; Ran, Q.; Dai, C.; Li, M.; Wang, M.: Geological conditions and exploration potential of shale oil in Qingshankou formation Northern Songliao Basin. Oil Gas Geol. **35**, 280–285 (2014)
44. Liu, C.; Wang, Z.; Guo, Z.; Hong, W.; Dun, C.; Zhang, X.; Li, B.; Wu, L.: Enrichment and distribution of shale oil in the Cretaceous Qingshankou formation, Songliao basin, northeast China. Mar. Pet. Geol. **86**, 751–770 (2017)
45. Liu, B.; Sun, J.; Zhang, Y.; He, J.; Fu, X.; Yang, L.; Xing, J.; Zhao, X.: Reservoir space and enrichment model of shale oil in the first member of cretaceous Qingshankou formation in the Changling sag, southern Songliao Basin NE China. Petroleum Explor. Develop. **48**(608), 624 (2021)
46. Liu, B.; Jin, L.; Hu, C.: Fractal characterization of silty beds/laminae and its implications for the prediction of shale oil reservoirs in Qingshankou Formation of northern Songliao Basin Northeast China. Fractals. **27**, 1940009 (2019)
47. Liu, B.; Yan, M.; Sun, X.; Bai, Y.; Bai, L.; Fu, X.: Microscopic and fractal characterization of organic matter within lacustrine shale reservoirs in the first member of Cretaceous Qingshankou Formation, Songliao Basin, Northeast China. J. Earth Sci. **31**, 1241–1250 (2020)
48. Liu, C.; Xu, X.; Liu, K.; Bai, J.; Liu, W.; Chen, S.: Pore-scale oil distribution in shales of the Qingshankou formation in the Changling Sag, Songliao Basin NE China. Marine and Petroleum Geol. **120**, 104553 (2020)
49. Feng, Z.; Zhang, S.; Fu, X.: Depositional evolution and accumulation response of Yaojia Nenjiang Formation in Songliao Basin. Earth Sci. Front. **19**, 78 (2012)
50. Zhang, L.; Bao, Z.; Dou, L.; Zang, D.; Mao, S.; Song, J.; Zhao, J.; Wang, Z.: Sedimentary characteristics and pattern of distributary channels in shallow water deltaic red bed succession: a case from the late cretaceous Yaojia formation, southern Songliao Basin, NE China. J. Petrol. Sci. Eng. **171**, 1171–1190 (2018)
51. Niu, B.; Bao, Z.; Yu, D.; Zhang, C.; Long, M.; Su, J.; Gao, X.; Zhang, L.; Zang, D.; Li, M.; Li, Y.: Hierarchical modeling method based on multilevel architecture surface restriction and its application in point-bar internal architecture of a complex meandering river. J. Petroleum Sci. Eng. **205**, 107378 (2021)
52. Zhang, L.; Bao, Z.; Dou, L.; Xu, Q.: Diagenetic alterations related to sedimentary architecture of deltaic distributary channels in red beds of the Cretaceous Yaojia Formation, Songliao Basin. J. Petroleum Sci. Eng. **203**, 108564 (2021)
53. Blattmann, T.; Liu, Z.; Zhang, Y.; Zhao, Y.; Haghipour, N.; Montluçon, D.; Plötze, M.; Eglinton, T.: Mineralogical control on the fate of continentally derived organic matter in the ocean. Science **366**(742–745), 6466 (2019)
54. Zhang, P.; Misch, D.; Meng, Q.; Sachsenhofer, R.F.; Liu, Z.; Jia, J.; Gao, F.; Bechtel, A.; Hu, F.: Lateral changes of organic matter preservation in the lacustrine Qingshankou formation cretaceous Songliao Basin NE China Evidence for basin segmentation. Int. J. Coal Geol. **254**, 103984 (2022)
55. Haq, B.U.: Cretaceous eustasy revisited. Glob. Planetary Change. **113**, 44–58 (2014)
56. Liu, B.; Song, Y.; Ye, X.; Zhu, K.; Yan, M.; Wan, L.; Li, C.; Li, Z.; Tian, W.: Algal-microbial community, paleoenvironment, and shale oil potential of lacustrine organic-rich shale in the upper cretaceous Nenjiang formation of the southern central depression, Songliao Basin (NE China). ACS Earth and Space Chem. **5**, 2957–2969 (2021)
57. Liu, B.; Wang, H.; Fu, X.; Bai, Y.; Bai, L.; Jia, M.; He, B.: Lithofacies and depositional setting of a highly prospective lacustrine shale oil succession from the upper cretaceous Qingshankou formation in the Gulong sag, northern Songliao Basin, northeast China. AAPG Bull. **103**, 405–432 (2019)
58. Zou, C.; Yang, Z.; Cui, J.; Zhu, R.; Hou, L.; Tao, S.; Yuan, X.; Wu, S.; Lin, S.; Wang, L.: Formation mechanism, geological characteristics and development strategy of nonmarine shale oil in China. Petroleum Explor. Develop. **40**, 15–27 (2013)
59. Miall, A.D.: Architectural-element analysis: a new method of facies analysis applied to fluvial deposits. Earth Sci. Rev. **22**, 261–308 (1985)
60. Peng, J.: Sedimentology of the upper pennsylvanian organic-rich cline shale, Midland Basin: from gravity flows to pelagic suspension fallout. Sedimentology **68**, 805–833 (2021)
61. Sing, K.S.: Reporting physisorption data for gas/solid systems with special reference to the determination of surface area and porosity. Pure Appl. Chem. **57**, 603–619 (1985)
62. Zhang, P.; Lu, S.; Li, J.; Xue, H.; Li, W.; Zhang, P.: Characterization of shale pore system: a case study of Paleogene Xin'gouzui formation in the Jianghan basin China. Marine and Petroleum Geol. **79**, 321–334 (2017)
63. Krohn, C.E.: Fractal measurements of sandstones, shales, and carbonates. J. Geophys. Res.: Solid Earth. **93**, 3297–3305 (1988)
64. Xiong, Z.; Cao, Y.; Liang, C.; Liu, K.; Wang, G.; Zhu, R.; Lei, P.; Wang, Y.: Origin and significance of authigenic quartz and albite in lacustrine calcareous fine-grained sedimentary rocks. Mar. Pet. Geol. **143**, 105799 (2022)

65. Ji, W.; Song, Y.; Jiang, Z.; Wang, X.; Bai, Y.; Xing, J.: Geological controls and estimation algorithms of lacustrine shale gas adsorption capacity: a case study of the Triassic strata in the southeastern Ordos Basin China. Int. J. Coal Geol. **134**, 61–73 (2014)
66. Liang, C.; Jiang, Z.; Cao, Y.; Zhang, J.; Guo, L.: Sedimentary characteristics and paleoenvironment of shale in the Wufeng-Longmaxi Formation, North Guizhou Province, and its shale gas potential. J. Earth Sci. **28**, 1020–1031 (2017)
67. Alonso-Zarza, A.M.; Wright, V.: Palustrine carbonates. Dev. Sedimentol. **61**, 103–131 (2010)
68. Zhu, X.; Zhang, M.; Zhu, S.; Dong, Y.; Li, C.; Bi, Y.; Ma, L.: Shale lithofacies and sedimentary environment of the third member, Shahejie Formation, Zhanhua Sag, Eastern China. Acta Geologica Sinica - English Edition. **96**, 1024–1040 (2022)
69. Heath, J.; Dewers, T.; McPherson, B.; Petrusak, R.; Chidsey, T., Jr.; Rinehart, A.; Mozley, P.: Pore networks in continental and marine mudstones: characteristics and controls on sealing behavior. Geosphere **7**, 429–454 (2011)
70. Peng, J.; Hu, Z.; Feng, D.; Wang, Q.: Sedimentology and sequence stratigraphy of lacustrine deep-water fine-grained sedimentary rocks: the Lower Jurassic Dongyuemiao Formation in the Sichuan Basin Western China. Mar. Pet. Geol. **146**, 105933 (2022)
71. Beitler, B.; Parry, W.; Chan, M.A.: Fingerprints of fluid flow: chemical diagenetic history of the Jurassic Navajo Sandstone, southern Utah, USA. J. Sedimentary Res. **75**, 547–561 (2005)